Earth System
Science
Data

Open Access · Discussions

1 **The Rocklea Dome 3D Mineral Mapping Test Data Set**

2 Carsten Laukamp[a], Maarten Haest[b], Thomas Cudahy[c]

3

4 [a]*CSIRO Mineral Resources, 26 Dick Perry Avenue, Kensington, WA 6151, Australia*

5 *(corresponding author: Carsten.Laukamp@csiro.au)*

6 [b]*MineSense Technologies, Vancouver, Canada*

7 [c]*C3DMM Pty Ltd, Perth, Australia*

8

9

10 **ABSTRACT**

11   The integration of surface and subsurface geoscience data is critical for efficient and

12 effective mineral exploration and mining. Publicly accessible datasets to evaluate the various

13 geoscience analytical tools and their effectiveness for characterisation of mineral assemblages

14 and lithologies or discrimination of ore from waste are however scarce. The open access

15 Rocklea Dome 3D Mineral Mapping Test Data Set (Laukamp, 2020;

16 https://doi.org/10.25919/5ed83bf55be6a) provides an opportunity for evaluating proximal and

17 remote sensing data, validated and calibrated by independent geochemical and mineralogical

18 analyses, for exploration of channel-iron deposits (CID) through cover. We present

19 hyperspectral airborne, surface and drill core reflectance spectra collected in the visible-near

20 infrared and shortwave infrared wavelength ranges (VNIR-SWIR; 350 to 2500 nm), as well as

21 whole rock geochemistry obtained by means of X-Ray fluorescence analysis and loss on

22 ignition measurements of drill core samples.

23   The integration of surface with subsurface hyperspectral data collected in the frame of

24 previously published Rocklea Dome 3D Mineral Mapping case studies demonstrated that about

25 30% of exploration drill holes were sunk into barren ground and could have been of better use,

26 located elsewhere, if airborne hyperspectral imagery had been consulted for drill hole planning.

27 The remote mapping of transported Tertiary detritals (i.e. potential hosts of channel iron ore

28   resources) versus weathered in situ Archaean geology (i.e. barren ground) has significant

29   implications for other areas where "cover" (i.e. regolith and/or sediments covering bedrock

30   hosting mineral deposits) hinders mineral exploration. Hyperspectral remote sensing represents

31   a cost-effective method for regolith landform mapping required for planning drilling programs.

32   In the Rocklea Dome area, vegetation unmixing methods applied to airborne hyperspectral

33   data, integrated with subsurface data, resulted in seamless mapping of ore zones from the

34   weathered surface to the base of the CID – a concept that can be applied to other mineral

35   exploration and mineral deposit studies. Furthermore, the associated, independent calibration

36   data allowed to quantify iron oxide phases and associated mineralogy from hyperspectral data.

37   Using the Rocklea Dome data set, novel geostatistical clustering methods were applied to the

38   drill core data sets for ore body domaining that introduced scientific rigour to a traditionally

39   subjective procedure, resulting in reproducible objective domains that are critical for the

40   mining process.

41   Beyond the already published case studies, the Rocklea Dome 3D Mineral Mapping

42   Test Data Set has the potential to develop new methods for advanced resource characterisation

43   and develop new applications that aid exploration for mineral deposits through cover. The here

44   newly presented white mica and chlorite abundance maps derived from airborne hyperspectral

45   highlight the additional applications of remote sensing for geological mapping and could help

46   to evaluate newly launched hyper- and multispectral spaceborne systems for geoscience and

47   mineral exploration.

48

49   **Key words**: Channel Iron ore Deposits, regolith, hyperspectral remote sensing, hyperspectral

50   drill core sensing, geochemistry

51 **1. INTRODUCTION**

52

53   The three dimensional (3D) geologic case history of the Rocklea Dome located in the

54 Hamersley Province (Western Australia) targeted the use of reflectance and emission

55 spectroscopy for measuring mineralogy and geochemistry specific to the exploration and

56 characterisation of economic Tertiary channel iron ore deposits in a terrain obscured by

57 weathered, transported materials. This public case history was generated by CSIRO's Western

58 Australian Centre of Excellence for 3D Mineral Mapping (C3DMM), which was operated from

59 2009 to 2012 and had the primary aim of generating and demonstrating the capabilities for

60 "scalable" 3D mineral mapping from the continental to the prospect scales (Cudahy, 2016).

61 The Rocklea Dome project was established in collaboration with Murchison Metal Ltd, who

62 granted C3DMM access to their drill hole dataset, consisting of 14 diamond cores and 180

63 reverse circulation drill holes. These drill holes were designed using traditional exploration

64 mapping technologies, such as published geology maps and geophysical data (magnetics and

65 radiometrics).

66   Key achievements of the Rocklea Dome 3D Mineral Mapping case study include:

67 • Based on the kaolin crystallinity index derived from surface and sub-surface

68   hyperspectral data (Cudahy, 2016), drill holes were identified that were sunk at surface

69   into barren (i.e. bedrock) weathered material. That is, approximately one third of the drill

70   holes need not have been drilled or would have been located differently had surface

71   mineral mapping data, e.g. airborne hyperspectral imagery, been used during drill hole

72   planning. This represents potential significant savings in time, money and environmental

73   disturbance.

74 • Characterisation of clay mineralogy associated with distinct domains of the CID and its

75   cover (i.e. kaolin group vs. Al-smectites vs. Fe-smectites) suggested that clay mineral

76   assemblages as well as calcrete atop buried CIDs have a different composition when

77   compared to regolith covering adjacent areas. That could represent useful information

78   when exploring for CIDs through regolith cover.

79   • Quantification of iron oxide phases and associated mineralogy derived from

80   hyperspectral data and validated using X-ray diffractometry and geochemistry (Haest et

81   al., 2012 a,b):

82   o iron (oxyhydr-)oxide content: RMSE of 9.1 weight % Fe

83   o Al clay content: RMSE 3.9 weight % Al_2O_3

84   o hematite/goethite ratio: RMSE 9.0 weight % goethite

85   o spatial characterisation of vitreous vs. ochreous goethite

86   • Geological modelling the iron ore resource of the Rocklea Dome CID (Haest et al., 2012

87   a,b; Cudahy, 2016; Fouedjio et al., 2018), which was reported by Dragon Resources in

88   2012 to be 72.6Mt (at 53% Fe cut-off) with 54.4% Fe, 7.2% SiO_2, 2.7% Al_2O_3, 0.031%

89   P and 11.2% LOI.

90   • Improvement of quality of mineral maps by application of vegetation unmixing methods

91   (Haest et al, 2013), resulting in seamless mapping of ore zones from the weathered

92   surface to the base of deposit (Cudahy, 2016).

93   All the above points showcase how hyperspectral data can be used for critical parts of

94   the mining cycle, especially exploration and 3D resource characterisation.

95   This article aims to provide an overview of the publicly available hyperspectral data set

96   of the Rocklea Dome, which ought to be used as a test data set for 1) data mining for exploration

97   and mining, 2) integration of independent geoscience data sets (i.e. hyperspectral,

98   geochemical), 3) resource modelling, and 4) different approaches for routine processing of

99   hyperspectral data.

100   The geological setting of the Rocklea Dome area, as well as analytical and processing

101   methods will be discussed first, after which the publicly available test data are listed as a table.

102   Example applications of the geochemical and mineralogical data for exploration, 3D mineral

103   mapping and Resource estimation are summarised briefly in the discussion.

104

105   **2. GEOLOGICAL SETTING**

106

107   The Rocklea Dome Channel Iron Deposit is located in the Hamersley Province, which

108   is the dominant source of Australia's iron ore exports. Channel Iron Deposits (CID) are

109   economically significant formations, providing a substantial percentage of the iron ore mined

110   in Australia. A detailed overview of the geology of the Rocklea Dome and the formation of the

111   CID was provided by Haest et al. (2012b) and is briefly summarised here. The bedrock geology

112   of the Rocklea Dome comprises a monzogranite pluton and cross-cutting mafic and ultramafic

113   intrusives that form part of the Pilbara Craton. The Archean age pluton is overlain by Archaean

114   to Proterozoic metasedimentary and volcanic rocks of the Hamersley Basin, enveloping the

115   central monzogranite dome (Fig. 1; Thorne & Tyler, 1996). Folding is attributed to

116   development of both the Ophthalmia and the Ashburton Fold Belt (Thorne & Tyler, 1996).

117   A meandering Tertiary palaeochannel passes over the Archean and Proterozoic rocks,

118   containing locally Channel Iron ore Deposits (CID), such as the Beasley River CID, which

119   crosscuts the north-western part of the Rocklea Dome. Channel iron ore was also drilled along

120   8 km strike length of a palaeochannel on the eastern side of the Rocklea Dome, which was

121   described by Haest et al. (2012a,b; 2013) as the Rocklea Dome CID (Figure 1). The bedrocks

122   and Tertiary channel are covered partly by regolith (e.g. Quaternary alluvium). Green

123   vegetation and dry vegetation (mostly Spinifex grass and bushes) cover the area partly.

124   A mixture of Fe-Ox pelletoids and ferruginised wood fragments below 10 mm in size

125   represent the major components of CIDs (Morris & Ramanaidou, 2007). In CID systems, the

126   base of the channel often consists of a clay horizon of variable composition. The CID is capped

127   in places by calcrete and silcrete.

128
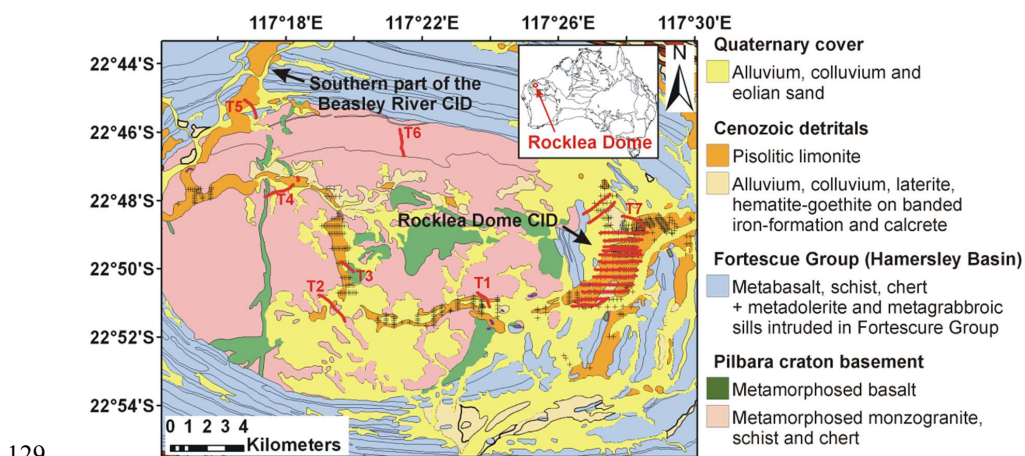
130   Figure 1: Geological map of the core of the Rocklea Dome (Haest et al., 2013; Thorne and
131   Tyler, 1996). Validation transects are indicated as red lines. T1 to T7 refer to transects
132   described in Haest et al. (2012a). The black crosses identify the position of all reverse
133   circulation drill cores intersecting the palaeochannel (i.e. pisolitic limonite in map) in the core
134   of the Rocklea Dome.

135

136   **3. METHODS AND MATERIALS**

137

138   *3.1.   VNIR-SWIR drill core spectroscopy*

139   Reflectance spectra of 180 rock chips (RC) and 14 diamond drill cores (RKD) were

140   measured using CSIRO's HyChips™ system (cf. Huntington et al., 2004), which comprises a

141   TerraSpec™-based spectrometer (Malvern-Panalytical) system. In total, 7,520 reflectance

142   spectra were collected from RC samples and 66,853 reflectance spectra were collected from

143   RKD samples (Haest et al., 2012a). An automated X-Y table moves the drill core tray in a

144   snake-like pattern below the TerraSpec optical fibre at a distance of ~6 to 13 cm (depending

145   on sample type, i.e., diamond core or drill chips), while the spectral data are collected. Each

146   sample spectrum is collected from a 1 × 1 cm area. Four light globes are positioned 40 cm

147   above and at a small angle (off the backscatter/specular angle) to the measurement/sample

148   point. In addition to hyperspectral data, high spatial resolution (0.1 mm pixel) images are

149   collected from the core or chip tray and the sample height in the tray is measured using a laser

150   profilometer. Reflectance spectra were calibrated using a Teflon/Spectralon™ panel (see Haest

151   et al., 2012a for more details). TerraSpec™ spectra were collected in the visible to near-

152   infrared (VNIR: 380−1,000 nm) and shortwave-infrared (SWIR: 1,000−2,500 nm), with

153   sampling intervals of 1.4 nm in the VNIR and 2.0 nm in the SWIR and a wavelength accuracy

154   of ±1 nm. The spectral resolution is 5 nm in the VNIR and between 11 and 12 nm in the SWIR.

155   The TerraSpec™ radiance spectra of each sample are first converted to apparent bidirectional

156   reflectance using the Teflon signal, which is collected at the beginning/end of each drill

157   core/drill chip tray measurement cycle. This signal is then converted to absolute reflectance,

158   based on the measurement of a Spectralon panel.

159

160   *3.2.   Remote Sensing*

161   Airborne VNIR–SWIR imagery was collected using the Airborne Multispectral

162   Scanner (AMS), which is an earlier version of HyVista Corporation's HyMap™ system (Cocks

163   et al., 1998). The AMS system collects 96 bands over the VNIR-SWIR, excluding the

164   atmospheric bands from ~1000 nm to ~1400 nm and from ~1800 to ~1950 nm, respectively.

165   For each spectral band, the average spacing of collected bands is 15 nm and the average full

166   width at half maximum is 17 nm. The AMS data over Rocklea Dome were collected in a north–

167   south direction between the 31st of July 2000 and the 2nd of August 2000, comprising a set of

168   14 flight lines, totalling in a combined length of ~280 km at a pixel size of approximately 7 m.

169   Atmospheric correction was done using MODTRAN5 (Berk et al., 2004, 2006) and SODA

170   (Rodger, 2011), based on a combination of the AMS at-sensor radiance with in-scene flight

171   parameters (e.g. latitude, longitude, sensor height, etc.). For more details about georeferencing

172   and mosaicking the single flight lines, see Haest et al. (2013).

173

174   *3.3.   X-ray fluorescence analysis (XRF)*

175   XRF analysis of 11,900 RC samples (1m interval) for weight percentages of Fe, P, S,

176   SiO_2, Al_2O_3, Mn, CaO, K_2O, MgO, and TiO_2 was conducted by Kalassay Ltd. (now Bureau

177   Veritas Minerals Pty Ltd., Western Australia). A Bruker Pioneer X-ray fluorescence instrument

178   with an end window 4 kW rhodium X-ray tube was used. Sample preparation included drying

179   at 105°C for 12 hr or for 1 hr, depending on whether the sample was wet or dry, respectively.

180   Samples were then crushed to a nominal 90% passing 75 μm. The sample powders were fused

181   in a Herzog automated (RF energized) fusion furnace and cast into 40 mm diameter beads using

182   a 12:22 flux containing 5% sodium nitrate. Matrix corrections were applied using a calculated

183   alpha correction for this combination of flux, tube, and instrument geometry. Previously

184   determined weight ranges were used for both the sample and the flux weight. Kalassay Ltd.

185   used lab duplicates, internationally certified reference materials, and reference materials of the

186   same ore type as standards and reported a precision better than 0.01% for all analyses. In order

187   to evaluate the accuracy of XRF analyses undertaken by Kalassay Ltd., duplicate samples were

188   also sent to the Amdel laboratory in Cannington (Western Australia), with good correlation

189   observed (Haest et al., 2012a).

190

191   *3.4.   Loss on ignition (LOI)*

192   In order to characterise the mineral assemblages present in the samples in more detail,

193   loss on ignition (i.e., LOI) measurements were undertaken on 11,900 RC samples to record the

194   mass loss of samples on heating (Haest et al., 2012a). A pre-dried portion of all samples was

195   heated in an electric furnace to 1,000°C. During this process, goethite will release its strongly

196   bonded water and its OH groups between 260° and 425°C (Strezov et al., 2010), organic matter

197   will be completely ignited by 550°C (Dean, 1974), aluminosilicate clay materials will

198   decompose between 530° and 605°C (Strezov et al., 2010), and inorganic carbon will be

199   oxidized and lost as CO_2 between 700° and 850°C (Dean, 1974).

200

201   *3.5.   Sample storage*

202   Drill core trays, field samples and XRF standards are all stored at the Australian

203   Resources Research Centre (ARRC) in Kensington (Western Australia). Samples can be

204   viewed and investigated at the ARRC, using local analytical facilities.

205

206   **4. SOFTWARE AND PROCESSING METHODS**

207   *4.1.   Processing of hyperspectral drill core data*

208   Hyperspectral drill core data were analysed using the CSIRO's The Spectral Geologist

209   software (TSG^{TM}) by interpreting the abundance, composition and/or crystallinity of selected

210   mineral groups and species using the Multiple Feature Extraction Method. A list of scripts

211   applied to the hyperspectral drill core and rock chip data can be found in Table 1.

212   Table 1: Base scripts and multiple feature extraction method scripts used for the Rocklea Dome

213   3D Mineral Mapping project.

Product name	Minerals detected	Base algorithm	Filters/Masks	Lower stretch limit	Upper stretch limit (only applicable for composition products)	related publication
Ferric oxide abundance (Ferric_oxide_abundance.txt)	Hematite, goethite, jarosite, "limonite"	Continuum removed depth of the 900 nm absorption calculated using a fitted 2nd order polynomial between 776 and 1050 nm $900/D$	R450 > R1650	0.04: low content		further developed on the basis of Haest et al. (2012a,b), which used a 4th order polynomial or 4 band ratio approach
Hematite-goethite distribution (Hematite-goethite_distr.txt)	Hematite-goethite ratio (Cudahy and Ramanaidou, 1997)	Continuum removed wavelength of the 900 nm absorption calculated using a fitted 2nd order polynomial between 776 and 1050 nm. $900W$	R450 > R1650 + 900D >0.025	~890nm: more hematitic	~910nm: more goethitic	further developed on the basis of Haest et al. (2012a,b), which used a 4th order polynomial or 4 band ratio approach
Ferrous iron abundance (Ferrous iron abundance.txt)	Fe^{2+} in silicates & carbonates, (Fe-chlorites, Fe-amphibole, Fe-pyroxene, Fe-olivine, Fe-carbonate)	$(R_{620}+R_{1650})/(R_{1027}+R_{1333})$ $Ferrous$		~1.005: low content		Laukamp et al. (2012)
opaques2 (opaques2inv.txt)	"Reduced" materials such as carbon black, sulphides and magnetite as well as Mn oxides.	albedo @ 1650 nm 1650	OPAQUES_450D1650 >0.25; albedo @ 1650 nm 1650 <30%	2: low content		
White mica and Al-smectite abundance (wmAlsmai.txt)	Abundance of white micas (e.g. illite, muscovite, paragonite, brammalite, phengite, lepidolite, margarite) and Al-smecites (montmorillonite, beidellite)	Relative absorption depth of the 2200 nm absorption for which the continuum is removed between 2120 and 2245, determined using a 3 band polynomial fit around the band with the lowest reflectance. $2200D$	$((R_{2138}+R_{2190})/(R_{2156}+R_{2379})$ 2160D2190 <1.063	0.02: low content		further developed on the basis of Sonntag et al. (2012), which used a 4th order polynomial or 4 band ratio approach
White mica and Al-smectite composition (wmAlsmci.txt)	Tschermak substitution of white micas, ranging from paragonite, brammalite, to illite, muscovite to phengite, and Al-smecites, ranging from beidellite to montmorillonite.	Minimum wavelength of the 2200 nm absorption for which the continuum is removed between 2120 and 2245, determined using a 3 band polynomial fit around the band with the lowest reflectance. $2200W$	$((R_{2138}+R_{2190})/(R_{2156}+R_{2379})$ 2160D2190 <1.063	2180 nm: Al-rich mica (muscovite, illite, paragonite, brammalite, lepidolite)	2220 nm: Al-poor mica (~phengite)	further developed on the basis of Sonntag et al. (2012), which used a 4th order polynomial or 4 band ratio approach
Kaolin abundance index	Kaolin group minerals, namely kaolinite halloysite, dickite and nacrite	2200D (Normalized depth of a fitted 4th order polynomial between 2120 and 2245 nm)	2160D ((R2138+R2190)/(R2156+R2179))>1.005	0.02: low content		Sonntag et al. (2012), Haest et al. (2012a,b)
Kaolin composition index	Composition and crystallinity of kaolin group minerals ranging from well-ordered kaolinite to halloysite to dickite (and nacrite)	[(R2138+R2173)/R2156]/[(R2156+R2190)/R2173]	2200D>0.005	low values = low crystallinity	high values = high crystallinity	Sonntag et al. (2012), Haest et al. (2012a,b)
Carbonates abundance (carbci3pfti.txt)	carbonates vs. MgOH-bearing silicates, based on left-asymmetry of CO3 feature @ 2340	Relative absorption depth of the 2340 nm absorption for which the continuum is removed between 2270 and 2370, determined using a 3 band polynomial fit around the band with the lowest reflectance. 2340D	2340D>0.04, 2295 nm<2340W<2360nm, 2250D< 0.025, 2380D>0.1117*2340D+0.0002. Asymmetry of the 2340 absorption using a fitted 4th order polynomial between 2120 and 2370: 2340_left_asym > 1.13	0.05: low content		further developed on the basis of Sonntag et al. (2012), which used a 4th order polynomial or 4 band ratio approach
Carbonate composition (carbci3pfti.txt)	separating calcite, dolomite, siderite, ...	Minimum wavelength of the 2340 nm absorption for which the continuum is removed between 2270 and 2370, determined using a 3 band polynomial fit around the band with the lowest reflectance. 2340W	2340D>0.04, 2295 nm<2340W<2360nm, 2250D< 0.025, 2380D>0.1117*2340D+0.0002. Asymmetry of the 2340 absorption using a fitted 4th order polynomial between 2120 and 2370: 2340_left_asym > 1.13	2303 nm: magnesite; 2326 nm: dolomite	2343 nm: calcite	further developed on the basis of Sonntag et al. (2012), which used a 4th order polynomial or 4 band ratio approach
White mica (+Al-smectite) abundance, refined for airborne hyperspectral imagery	Abundance of white micas (e.g. illite, muscovite, paragonite, brammalite, phengite, lepidolite, margarite) and Al-smecites (montmorillonite, beidellite)	Relative absorption depth of the 2200 nm absorption for which the continuum is removed between 2120 and 2245, determined using a 3 band polynomial fit around the band with the lowest reflectance. $2200D$	$((R_{2138}+R_{2190})/(R_{2156}+R_{2379})$ 2160D2190 <1, 2200D2320D > 1.5	0.04: low content	0.255: high content	further developed on the basis of Sonntag et al. (2012), which used a 4th order polynomial or 4 band ratio approach
Chlorite (+epidote, +biotite) abundance, refined for airborne hyperspectral imagery	Abundance of chlorite (e.g. clinochlore, chamosite), as well as members of the epidote and biotite mineral groups	(R2227+R2275)/(R2241+R2259), $2254D$	2250D> 1.01, & 2300 < 2320W <2342 & 2240 <2250W < 2260	1.01: low content	1.04: high content	further developed on the basis of Sonntag et al. (2012)

214

Earth System
Science
Data
Open Access
Discussions

215

4.2. Image Processing

216

217 The processing strategy for generating geoscience products from AMS data, such as the

218 Kaolin Crystallinity (Table 1) builds on the quality control of the acquired data (Cudahy et al.,

219 2008). Well calibrated radiance-at-sensor or surface reflectance data are required for the

220 processing of airborne hyperspectral imagery. Commonly applied levelling and statistics-based

221 methods were avoided as these introduce undesirable scene-dependencies, making a

222 comparison of image products from different areas impossible. Physics-based reduction

223 models were applied to the remote sensing data, using the image processing software ENVI^{TM}.

224 Complicating effects were removed in their order of development (i.e. 1. instrument, 2.

225 atmospheric, 3. surface effects) through either normalization or offsets.

226

4.3. The Multiple Feature Extraction Method

227

228 In hyperspectral proximal (e.g. HyLogging^{TM}) and remote (e.g. AMS) sensing

229 technologies, the VNIR, SWIR, and thermal infrared (TIR: ca. 6000 – 14500 nm) wavelength

230 ranges are used to infer abundance and composition of various geological materials. The

231 relative intensity and wavelength position of absorption features in the reflectance spectra

232 relate to the physicochemical characteristics of the various minerals. Feature extraction

233 methods can be used to determine the mineralogy of a sample material (Cudahy et al., 2008).

234 The advantage the multiple feature extraction method (MFEM) is that the associated scripts

235 are not biased on a training dataset or spectral reference libraries, but are based only on the

236 visible and/or infrared active functional groups of minerals (see Laukamp et al., 2011, for more

237 details). As they are instrument independent, the same scripts can be applied to remote sensing

238 and proximal hyperspectral data, easing the integration of, for example, surface (e.g. HyMap)

239 and subsurface data (e.g. HyLogging^{TM}) for the purpose of visualisation in 3D or advanced

240   data analytics. Interferences of mineralogical information with other surface materials such as

241   vegetation can be evaluated by using a multiple linear regression model for unmixing

242   vegetation from hyperspectral remote sensing data (Rodger & Cudahy, 2009; Haest et al.,

243   2013). Other complications, such as spectrally overlapping materials, are removed by the

244   application of thresholds.

245

246   **5. DATA PRODUCTS AND APPLICATIONS**

247   Publicly accessible data of the Rocklea Dome 3D Mineral Mapping project can be

248   found   on   CSIRO's   Data   Access   Portal:

249   https://data.csiro.au/collections/#collection/CIcsiro:44783

250   (https://doi.org/10.25919/5ed83bf55be6a) and are listed in Table 2. Data and other content on

251   this site are scientific research data collected by CSIRO and third parties and are made available

252   on an 'as is' basis. If any data or other material are downloaded from this site, the user does so

253   at own risk and acknowledges that such data or other content: 1) may contain general

254   statements based on scientific research and may be incomplete and not applicable to all

255   situations; 2) is not professional, scientific, medical, technical or expert advice and is subject

256   to the usual uncertainties of scientific and technical research; and 3) should not be relied upon

257   as specific to you and therefore as the basis for doing or failing to do something. Expert

258   professional scientific and technical advice should be sought prior to acting in reliance on data

259   and other material from this site. To the extent permitted by law, CSIRO excludes all liability

260   to any person for any consequences, including but not limited to all losses, damages, costs,

261   expenses and any other compensation, arising directly or indirectly from using and any

262   information or material contained in it.

263

264   Table 2: Publicly accessible data of the Rocklea Dome 3D Mineral Mapping project

265   (https://data.csiro.au/collections/#collection/CIcsiro:44783;

266   https://doi.org/10.25919/5ed83bf55be6a)

main directory	sub directory	file name	type of data	source/IP
DTM		DTM_Rocklea_50k.00t	Digital terrain model	GSWA
		DTM_Rocklea_50k.dxf		
		DTM_Rocklea_50k.evf		
		DTM_Rocklea_50k.zip		
		Hardey_HR_DTM.00t	Digital terrain model of 100K mapsheet Hardey 2252	GSWA
		Hardey_HR_DTM.dxf		
		Hardey_HR_DTM.evf		
		Topography_ENVI	Digital elevation model	GSWA
		Topography_ENVI.hdr		
		dem_plus_collars.csv	Digital elevation model	GSWA
drill hole data	RC_hyperspectral_geochem	GeoscienceProductDescriptions_ProximalHyperspectral.xlsx	table describing multiple feature extraction scripts applied to hyperspectral data for interpretation of mineralogy	CSIRO
		RC_data.tsg	TSG-file	CSIRO
		RC_data.ini	TSG-file	CSIRO
		RC_data.bip	TSG-file	CSIRO
		RC_data_cras.bip	TSG-file	CSIRO
		RC_data_tsgexport.CSV	spectral and geochemical data exported from TSG	CSIRO
	RKD	RKD5-7-9.tsg	TSG-file	CSIRO
		RKD5-7-9.ini	TSG-file	CSIRO
		RKD5-7-9.bip	TSG-file	CSIRO
		RKD5-7-9_cras.bip	TSG-file	CSIRO
remote sensing data	GeoTIFF_AMS/	2200D_Mstd.tfw	AMS product "2200D", showing the relative abundance of Al-clays	CSIRO
		2200D_Mstd.tif		CSIRO
		2200WAR_2190-2205.tfw	AMS product "2200W", indicating compositional changes of Al-smectites and white micas ($Al^{VI}Al^{IV}(Fe,Mg)_{-1}Si_{-1}$)	CSIRO
		2200WAR_2190-2205.tif		CSIRO
		2250_MStd.tfw	AMS product "2250D", showing the relative abundance of chlorite, epidote and/or biotite	CSIRO
		2250_MStd.tif		CSIRO
		2330_2250-2380.tfw	AMS product "Carbonate abundance", showing the relative abundance of carbonates	CSIRO
		2330_2250-2380.tif		CSIRO
		KC_NoSM_22D+216DM_3MeFi.tfw	AMS product "Kaolin crystallinity"	CSIRO
		KC_NoSM_22D+216DM_3MeFi.tif		CSIRO
	TXT_AMS/	2320D_vegunm.txt	AMS product "2320D", vegetation unmixed	CSIRO
		AlOHAbVegunm.txt	AMS product "Al-clay abundance index", vegetation unmixed	CSIRO
		FeOxVegUnm.txt	AMS product "Ferric Oxide Abundance Index", vegetation unmixed	CSIRO
		SRTM_RockleaDome+HardeyRiver.txt	Digital elevation model	GSWA

Earth System
Science
Data
Open Access
Discussions

	StudentExercises_Rocklea.docx	Exercises for analysis of HyLogging data	CSIRO
Rocklea Dome exercise	Answers_CIDexercises.docx	Suggested answers to exercises for analysis of HyLogging data	CSIRO
	MinSpec_Workshop_7RockleaDomeTSG_HandsOn.pptx	PPT-presentation summarising Rocklea Dome exercise and results	CSIRO

267

268   The following chapters briefly describe examples of how the provided hyperspectral

269   and geochemical proximal and remote sensing data sets can be used to address challenges for

270   the mineral resources sector.

271

272   *5.1.   Drill core mineralogy and geochemistry*

273   Reflectance spectra collected from rock chips (RC) and diamond drill cores (RKD)

274   using CSIRO's HyChips™ system presented a cost-effective way to spatially map the major

275   ore (i.e. goethite +/- hematite) and gangue minerals (i.e. kaolinite, smectite, carbonate), apart

276   from quartz, in detail. To achieve this, the relative intensity of mineral-diagnostic absorption

277   features was calculated using a suite of batch scripts ("Geoscience Products" in Haest et al.,

278   2012a). The relative intensity of the respective absorption features correlates with the relative

279   abundance of the respective mineral, whereas the wavelength position of key absorption

280   features relates to mineral speciation (e.g. ochreous versus vitreous goethite) or determining

281   the mineral chemistry. For example, the relative abundance of iron oxides was calculated from

282   the relative depth of the ferric iron-related absorption at around 900 nm (Cudahy &

283   Ramanaidou, 1997), whereas goethite was distinguished from hematite by tracking the

284   wavelength position of the same absorption feature (Table 2 in Haest et al., 2012a).

285   Whole rock geochemistry obtained from the same drill core material showed significant

286   correlations with the Geoscience Products. Haest et al. (2012) determined an RMSE of 9.1

287   weight % Fe for the correlation between the hyperspectrally-derived iron oxide abundance and

288   the XRF weight % Fe data and an RMSE of 3.9 weight % Al_2O_3 for correlation between the

289   hyperspectrally-derived Al-clay abundance and the XRF weight % Al_2O_3 data. The errors

290   associated with the correlations were found to be due to a combination of grain size variations

291   and the transopaque behaviour of iron oxides and/or different amounts of silica, causing

292   variations in the optical depth of sample material.

293

294   *5.2.   Surface mineral mapping*

295   Airborne hyperspectral surveys provide spatially contiguous mineralogical information

296   of the Earth's surface at high spatial resolution (down to circa 1 m). The relative intensity of

297   mineral diagnostic absorption features and their wavelength positions can be used to infer the

298   relative abundance of the respective minerals and even variations of single mineral species in

299   terms of their cation composition, crystallinity and hydroxylation. The Rocklea Dome case

300   study data set was used by Haest et al. (2013) to demonstrate how quantitative mineral maps

301   can be produced by validation of airborne hyperspectral data against field data, including

302   reflectance spectra and XRF data collected from surface samples. The effect of both green and

303   dry vegetation cover was unmixed at the pixel-level using the Normalised Difference

304   Vegetation Index (NDVI; e.g. Tucker, 1979) and the continuum-removed depth of the

305   cellulose-lignin absorption centred at around 2100 nm, respectively. The resulting mineral

306   mapping products have a higher spatial continuity, as well as higher accuracy of, for example,

307   mineral abundance or composition values shown in single pixels. This proved to be especially

308   useful in areas with outcropping CID, which appeared to be sub-economic from the original

309   iron oxide abundance mineral maps but showed as potentially economic CID resources when

310   the vegetation cover was unmixed (Figure 2).

311
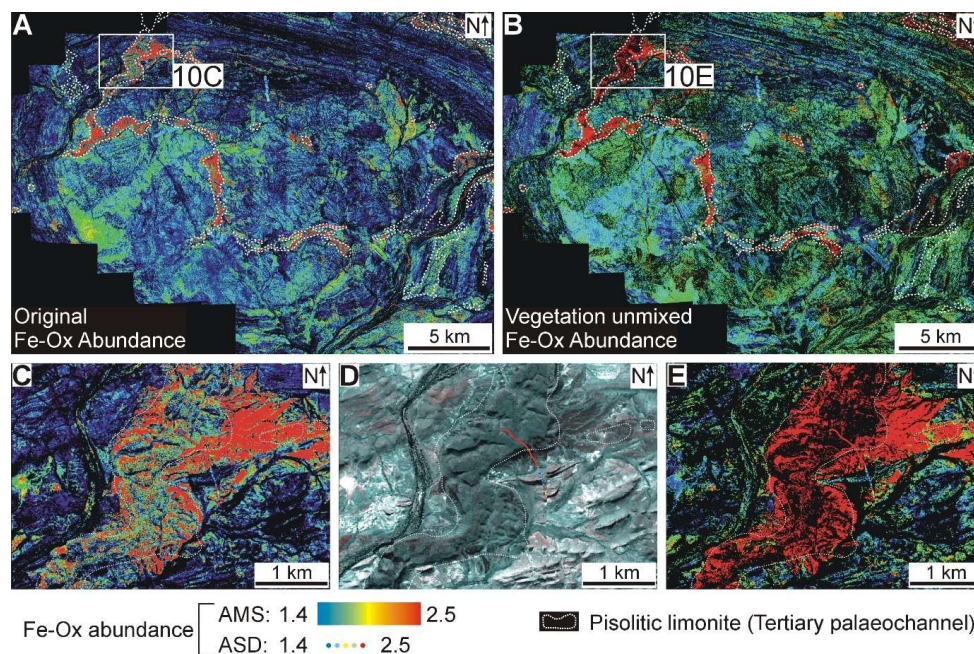
Figure 2: A–B: Fe-(oxyhydr-)oxide (Fe-Ox) abundance maps of the Rocklea Dome without
(A) and with (B) vegetation unmixing. C–E: Fe-Ox abundance maps of the southern part of
the Beasley River CID with (C) and without (E) vegetation removal and the false colour
image of this area (D). The Beasley River CID has a plateau like surface expression, with the
edges of the plateau clearly visible in the false colour image. These edges where mapped by
the Geological Survey of Western Australia as representing the boundary of the pisolitic
limonite (Fe-rich palaeochannel; white stippled line) (the Fe-Ox abundance measurements
collected along transects 1 to 7 with the TerraSpec[TM] are also shown for reference).

320

321   Beyond the iron oxide, kaolin and carbonate mineral maps published by Haest et al.

322 (2013), airborne hyperspectral data can be used to create numerous additional mineral mapping

323 products that can be used to address other geoscientific questions. For example, the Rocklea

324 Dome presents a wide variety of igneous units that are part of the Proterozoic basement of the

325 Pilbara Craton (Figure 1). These include 1) metamorphosed monzogranite, schist and chert, 2)

326 metamorphosed basalt, and 3) amphibolite dykes. According to the white mica abundance

327 derived from airborne hyperspectral data (green in Figure 3a), the metamorphosed

328 monzogranite contains less white mica, when compared to the metamorphosed schists which

329   are striking East-West and occur in the northern part of the Rocklea Dome (red in Figure 3a).

330   In the eastern half of the Proterozoic basement in the Rocklea Dome, white mica is much less

331   abundant to absent. This coincides with elevated amounts of chlorite (folded lithologies in the

332   centre of Figure 3b), which map out metamorphosed basalt (Figure 1). The North-South

333   striking occurrence of chlorite in the Western half of the Proterozoic basement traces an

334   amphibolite dyke. Both the white mica abundance and chlorite abundance maps can also be

335   used to map out different lithologies in the metasediments and metabasalts of the Fortescue

336   that crop out to the North and South of investigated area, demonstrating how the airborne

337   hyperspectral data can be used to map out all major lithologies occurring in the Rocklea Dome

338   case study area.

339
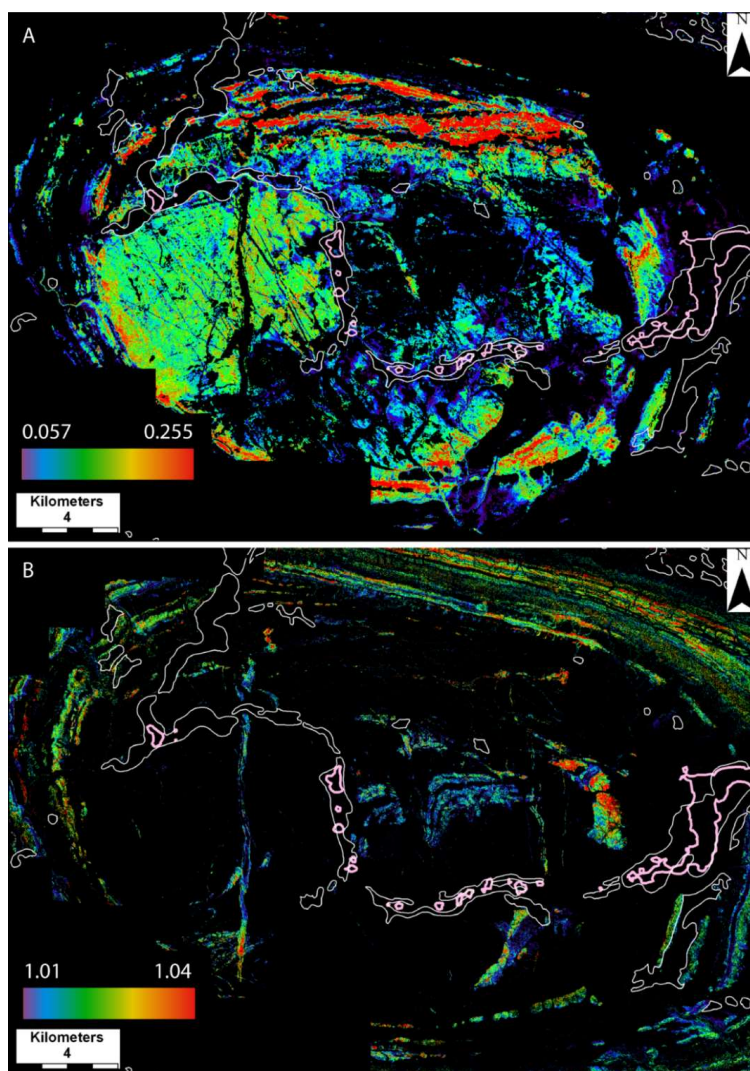
Figure 3: A & B: White mica (+Al-smectite) and chlorite (+epidote, +biotite) abundance
maps of the Rocklea Dome area in A and B, respectively, calculated from airborne
hyperspectral data using algorithms described in Table 1. Warm colours represent high
abundance and cool colours low abundance of the respective minerals. Black pixels have
been masked out as relative intensity of the absorption feature mapped in the respective
mineral map is below a given threshold (Table 1) and/or because of non-mineralogical effects
(e.g. vegetation, clouds). A shows monzogranites in the western part of the dome in green
colours and the Fortescue Group in the northern fringe of the dome in red colours. B
highlights Archean metamorphosed basalts in the eastern part of the dome structure and an N-
S trending amphibolite dyke in the western part of the dome. White lines indicate the surface
extension of the Tertiary channel as mapped by Thorne & Tyler (1996). Pink lines indicate
the horizontal extension of the Tertiary channel as mapped by the hyperspectral data.

352

5.3.   3D Mineral Mapping

354   The hyperspectral drill core data can be combined with airborne hyperspectral data into

355   a seamless 3D mineral model of the Rocklea Dome CID (Figure 4). For this, all hyperspectral

356   data were resampled to the same spatial resolution and imported into the 3D modelling software

357   GoCad/SKUA™. The channel basement contact that was delineated at depth using the kaolin

358   crystallinity products could also be delineated at the surface from the airborne hyperspectral

359   image. A combination of both provided a seamless surface of the channel bottom (grey surface

360   in Figure 4) that separates the basement characterised by well-crystalline kaolinite from the

361   tertiary channel sediments characterised by poorly-crystalline kaolinite. The here identified

362   channel basement contact deviates at the surface significantly from the area mapped by the

363   geological survey as palaeochannel. This suggests that drilling patterns could have been much

364   better defined if the airborne hyperspectral-based surface outline would have been available

365   prior to drilling (Cudahy, 2016).

366   As part of their 3D Geomodel Series, the Geological Survey of Western Australia

367   (GSWA) provides access to 3D models of the Rocklea Dome area via their online portal:

368   https://dmpbookshop.eruditetechnologies.com.au/product/rocklea-inlier-2016-3d-geomodel-

369   series.do. The data can be viewed in three different formats (3D PDF, Geoscience Analyst,

370   GOCAD).

371

20
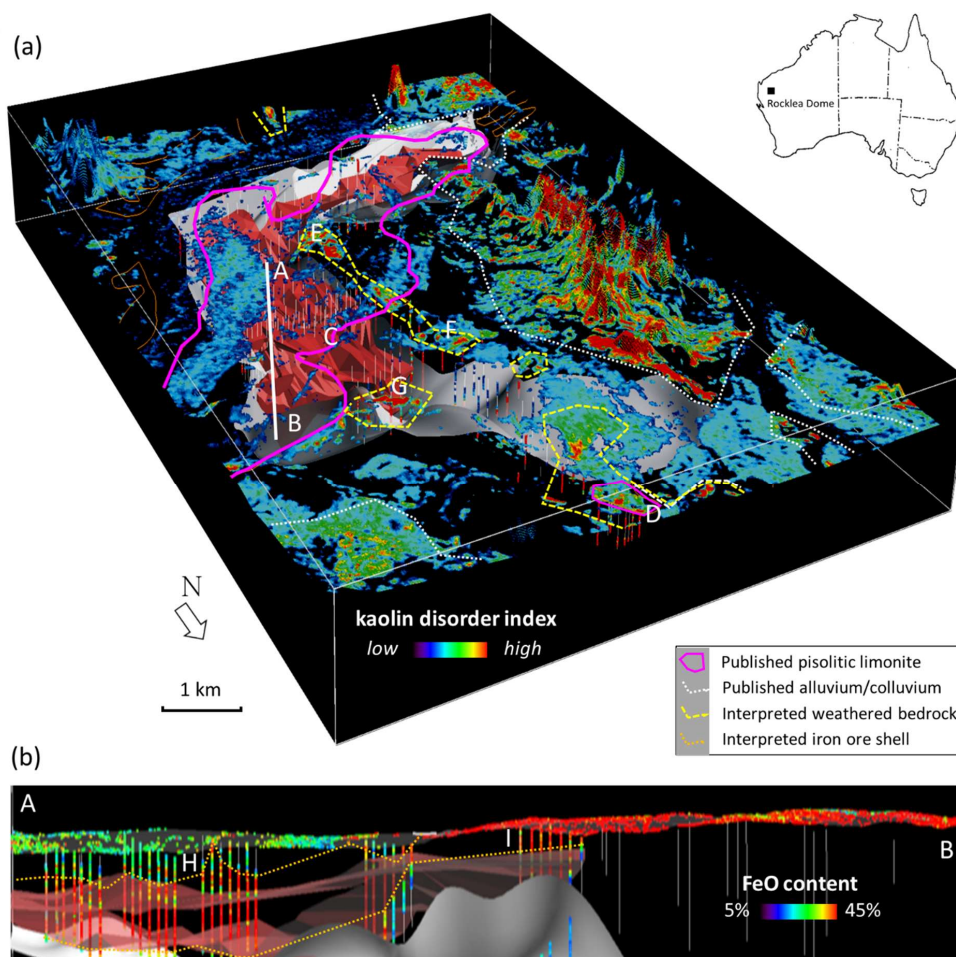
Figure 4: 3D mineral models of the Rocklea Dome area (Cudahy, 2016). Scene centre is approximately 22.8216° latitude 117.4652° longitude. (a) A southwest oblique 3D view of the Rocklea Dome study area showing kaolin disorder measured using airborne HyMap™ (surface) and drill core HyLogger™ (coloured vertical pegs) reflectance spectra. Warmer colours (well-ordered kaolin) relate to weathered, in situ bedrock, while cooler colours (poorly-ordered kaolin) relate to transported (alluvium/colluvium) materials. The interpolated model of the base of the channel iron system calculated using the 3D kaolin crystallinity map is shown by the shaded grey surface. The CID, which was calculated from the XRF-derived % FeO (Haest et al., 2012a), is shown by a shaded red volume. Areas of weathered bedrock (as mapped by Haest et al., 2012b and Cudahy, 2016) are highlighted by yellow-coloured hashed lines and highlight which drill cores were sunk into barren ground. A white straight line shows the location of the cross-section (A–B) presented in (b); (b) Cross section A–B in (a) of the % FeO measured from the drill core and airborne imagery, which was vegetation unmixed (Haest et al., 2013).

21

387

388   *5.4.   Resource estimation*

389   Resource estimation of base and precious metal deposits requires the grouping of drill

390   hole data into domains that represent zones of homogenous properties for accurate grade

391   estimation and practical exploitation purposes. In practice, this is more than often performed

392   through a subjective time-consuming manual interpretation of sample analytical data.

393   Traditional automated clustering techniques, such as multivariate clustering and k-means, tend

394   to show poor spatial contiguity of domains in a mineral deposit. Fouedjio et al. (2017) used the

395   Rocklea Dome drill core data set to showcase how geostatistical clustering methods can take

396   spatial dependency into account (Figure 5). By integrating whole rock geochemistry and

397   hyperspectral drill core data, Fouedjio et al. (2017) revealed two distinct domains in the

398   Rocklea Dome Channel Iron Ore Deposit that are mainly characterised by four geochemical

399   variables (FeO, Al_2O_3, SiO_2 and TiO_2) and two mineralogical variables derived from

400   hyperspectral data (ferric oxide abundance and kaolinite abundance). Ore body domaining

401   through geostatistical clustering represents a method for objective samples clustering that

402   introduces scientific rigour to a traditionally subjective procedure. The robust domaining is

403   based in genuine multivariate geostatistics combining all available data. The flexible and

404   reproducible automatic domaining technique saves time, improves the understanding of

405   domains critical for exploitation of the ore and allows an easy integration of new data sets.

406
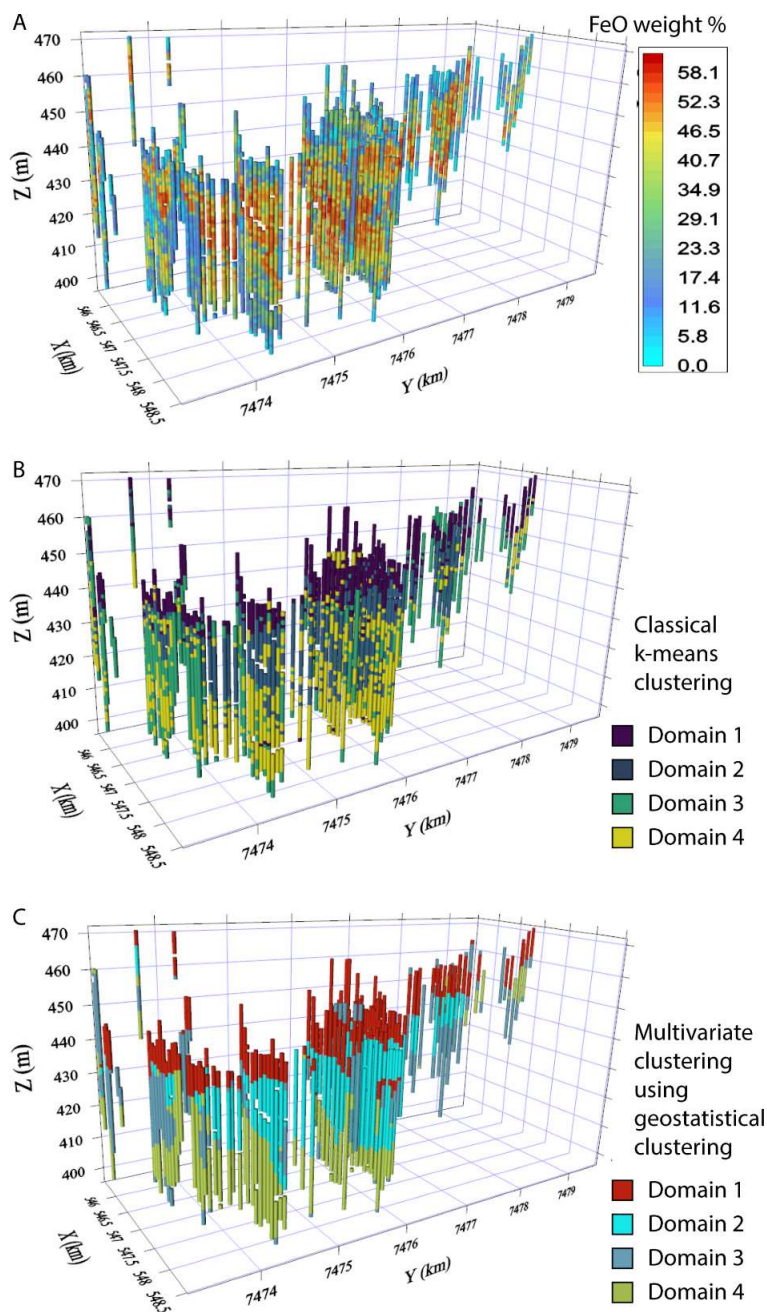
Figure 5: a) Spatial plot of FeO distribution in the Rocklea Dome Chanel Iron Deposit. (b) Classical k-means clustering method using 4 domains. (c) Geostatistical spectral clustering using 4 domains. Z-axis was scaled to ease visualisation. Modified from Fouedjio et al. (2017).

412

413

414

415   *5.5.   Teaching material*

416   The publicly available Rocklea Dome data set provided an opportunity to compile

417   training and teaching material about the application of hyperspectral drill core and chips data

418   for iron ore resource characterisation using The Spectral Geologist Software (TSG^{TM};

419   https://research.csiro.au/thespectralgeologist/). Student exercises and example answers, as well

420   as a ppt for teaching are part of the data package:

421   Exercise: StudentExercises_Rocklea.docx

422   Answers: Answers_CIDexercises.docx

423   PPT for teaching: MinSpec_Workshop_7RockleaDomeTSG_HandsOn.pptx

424

425   **6. CONCLUSIONS AND OUTLOOK**

426   We have established an open-access dataset comprising drill core, surface and airborne

427   hyperspectral data of the Rocklea Dome area in the Hamersley Basin of Western Australia,

428   which features a wide variety of lithologies and morphologies and is prospective for channel-

429   hosted iron ore resources. The proximal and remote sensing data, together with associated

430   whole rock geochemistry are ideal for researching the geology of this economically significant

431   area and allow a thorough comparison of different geoanalytical techniques and their

432   effectiveness for resource characterisation. Combining the surface and subsurface data into 3D

433   mineral maps provides a better visual understanding of the geological environment.

434   In addition to the already published surface and subsurface mineral mapping products,

435   many more Geoscience Products can be generated to better understand this geologically

436   complex area. The here newly presented white mica and chlorite abundance maps clearly

24

437 highlight the potential for mapping out different sections of the Archaean monzogranitic

438 basement as well as different generations of mafic intrusives. Of particular interest are the

439 contact zones between the mafic dykes and their host rocks, as they could help to better

440 understand the intensity of alteration within the dyke and within the host granite as well as the

441 associated fluid-rock interaction processes.

442 The teaching material provided together with this open-access dataset aims to support

443 training of geoscience graduates and post-graduates in the potential applications of

444 hyperspectral proximal and remote sensing data for mineral exploration and resource

445 characterisation.

446 All analytical technologies used for collection of the geoscience data, as well as

447 software packages used for processing the data, are commercially available. However, it should

448 be noted that the HyChips™ system is now superseded by HyLogger3, which collects thermal

449 infrared wavelengths (TIR; 6000 to 14500 nm) in addition to the VNIR-SWIR data. The

450 collection of the TIR wavelength range enables the characterisation of major rock forming

451 minerals such as quartz, which are of major importance for characterisation of iron ore

452 resources, but were not detectable with HyChips^{TM}. The HyLogger3 technology is in operation

453 at the six nodes of the Australian National Virtual Core Library

454 (https://www.auscope.org.au/nvcl), which provides online open access to more than 3,500 drill

455 cores from the Australian continent.

456

457 **7. DATA AVAILABILITY**

458 The supplement related to this article is available online at:

459 https://doi.org/10.25919/5ed83bf55be6a (Laukamp, 2020). A 3D model of the Rocklea Dome

460 data set is also available from the Geological Survey of Western Australia:

461 https://dasc.dmp.wa.gov.au/DASC?productAlias=Rocklea3D.

Earth System
Science
Data

Discussions

462

8. AUTHOR CONTRIBUTIONS

463

464 CL, TC and MH contributed equally to the manuscript preparation. CL is the custodian

465 of the Rocklea Dome data set stored on the CSIRO's Data Access Portal.

466

9. COMPETING INTERESTS

467

468 The authors declare that they have no conflict of interest.

469

10. ACKNOWLEDGEMENTS

470

481

482

REFERENCES

483

484 Berk, A., Anderson, G. P., Acharya, P. K., Bernstein, L. S., Muratov, L., Lee, J., et al. (2006).

485 MODTRAN (TM) 5: 2006 update — art. no. 62331F. In S. S. L. P. E. Shen (Ed.), Algorithms

486 and technologies for multispectral, hyperspectral, and ultraspectral imagery, XII Pts 1 and 2. (pp.

487 F2331–F).

Earth System
Science
Data

Open Access

Discussions

488 Berk, A., Cooley, T. W., Anderson, G. P., Acharya, P. K., Bernstein, L. S., Muratov, L., et al. (2004).

489 MODTRAN5: a reformulated atmospheric band model with auxiliary species and practical

490 multiple scattering options. In K. P. C. A. C. M. R. P. R. H. S. N. I. Schafer (Ed.), Remote sensing

491 of clouds and the atmosphere, Ix. (pp. 78–85).

492 Cocks, T., Jenssen, R., Stewart, A., Wilson, I., & Shields, T. (1998). The HyMap™ airborne

493 hyperspectral sensor: The system, calibration and performance. 1st EARSEL Workshop on

494 Imaging Spectroscopy, Zurich, October 1998 (http://www.neodc.rl.ac.uk/docs/

495 Hymap_specs.pdf)

496 Cudahy, T.J., 2016, Mineral Mapping for Exploration: An Australian Journey of Evolving Spectral

497 Sensing Technologies and Industry Collaboration. Geosciences 2016, 6, 52;

498 doi:10.3390/geosciences6040052

499 Cudahy, T.J., and Ramanaidou, E.R., 1997, Measurement of the hematite: goethite ratio using field

500 visible and near-infrared reflectance spectrometry in channel iron deposits, Western Australia:

501 Australian Journal of Earth Sciences, v. 44, p. 411−420.

502 Cudahy, T., Jones, M., Thomas, M., Laukamp, C., Caccetta, M., Hewson, R., Rodger, A., Verrall, M.

503 (2008): Next Generation Mineral Mapping: Queensland airborne HyMap and satellite ASTER

504 surveys 2006-2008.- CSIRO report P2007/364, 161pp.

505 Dean, W.E., 1974, Determination of carbonate and organic-matter in calcareous sediments and

506 sedimentary-rocks by loss on ignition—comparison with other methods: Journal of Sedimentary

507 Petrology, v. 44, p. 242−248.

508 Fouedjio, F., Hill, E.J., Laukamp, C. (2018): Ore Body Domaining through Geostatistical Clustering:

509 Case Study at the Rocklea Dome Channel Iron Ore Deposit, Western Australia.- Applied Earth

510 Science, Volume 127(1), 15-29.

511 Haest, M., Cudahy, C., Rodger, A., Laukamp, C., Martens, C., Caccetta, M. (2013): Unmixing

512 vegetation from airborne visible-near to shortwave infrared spectroscopy-based mineral maps

513 over the Rocklea Dome (Western Australia), with a focus on iron rich palaeochannels.- Remote

514 Sensing of Environment, 129, 17-31.

515   Haest, M., Cudahy, T., Laukamp, C., Gregory, S. (2012a): Quantitative mineralogy from visible to
516   shortwave infrared spectroscopic data - I. Validation of mineral abundance and composition
517   products of the Rocklea Dome channel iron deposit in Western Australia.- Economic Geology,
518   107, 209 - 228.

519   Haest, M., Cudahy, T., Laukamp, C., Gregory, S. (2012b): Quantitative mineralogy from visible to
520   shortwave infrared spectroscopic data - II. 3D mineralogical characterisation of the Rocklea
521   Dome channel iron deposit, Western Australia - Economic Geology, 107, 229 - 249.

522   Haest, M., Cudahy, T., Laukamp, C. (2012c): Application of infrared spectroscopy-based mineralogy
523   to channel iron ore resource evaluation.- Resource Evaluation and Mining 2012, 30.03.2012,
524   Perth, 29-33.

525   Huntington, J., Mauger, A., Skirrow, R., Bastrakov, E., Connor, P., Mason, P., Keeling, J., Coward, D.,
526   Berman, M., Phillips, R., Whitbourn, L., Heithersay, P., and AusIMM, 2004, Automated
527   mineralogical logging of core from the Emmie Bluff, iron oxide copper-gold prospect, south
528   Australia, Pacrim 2004 Congress, 2004: Parkville Victoria, Australasian Institute of Mining and
529   Metallurgy Publication Series, p. 223−230.

530   Laukamp, C., Cudahy, T., Caccetta, M., Chia, J., Gessner, K., Haest, M., Liu, Y.C., Rodger, A. (2010):
531   The uses, abuses and opportunities for hyperspectral technologies and derived geoscience
532   information.- AIG Bulletin, 51(Geo-Computing 2010 Conference, Brisbane, September 2010):
533   73-76.

534   Laukamp, C. (2011): Short Wave Infrared Functional Groups of Rock-forming Minerals.- CSIRO
535   report EP115222.

536   Laukamp,   C.   (2020):   Rocklea   Dome   C3DMM.   v1.   CSIRO.   Data   Collection.
537   https://doi.org/10.25919/5ed83bf55be6a

538   Morris, R. C., & Ramanaidou, E. R. (2007). Genesis of the channel iron deposits (CID) of the Pilbara
539   region, Western Australia. Australian Journal of Earth Sciences, 54, 733–756.

540   Ramanaidou, E.R., Morris, R.C., and Horwitz, R.C., 2003, Channel iron deposits of the Hamersley
541   Province, Western Australia: Australian Journal of Earth Sciences, v. 50, p. 669−690.

542   Rodger, A. (2011). SODA: A new method of in-scene atmospheric water vapor estimation and post-

543   flight spectral recalibration for hyperspectral sensors: Application to the HyMap sensor at two

544   locations. Remote Sensing of Environment, 115, 536–547.

545   Rodger, A. & Cudahy, T. (2009): Vegetation corrected continuum depths at 2.20 mm: An approach for

546   hyperspectral sensors.- Remote Sensing of Environment, 113: 2243-2257.

547   Sonntag, I., Laukamp, C., Hagemann, S. (2012): Low potassium hydrothermal alteration in low

548   sulfidation epithermal systems as detected by IRS and XRD: an example from the Co-O Mine,

549   Eastern Mindanao, Philippines.- Ore Geology Reviews, 45, 47-60.

550   Strezov, V., Ziolkowski, A., Evans, T.J., and Nelson, P.F., 2010, Assessment of evolution of loss on

551   ignition matter during heating of iron ores: Journal of Thermal Analysis and Calorimetry, v. 100,

552   p. 901−907.

553   Thorne, A.M., & Tyler, I.M. (1996). Geology of the Rocklea 1:100000 sheet. Perth: Western Australia

554   Geological Survey.

555   Tucker, C. J. (1979). Red and photographic infrared linear combinations for monitoring vegetation.

556   Remote Sensing of Environment, 8, 127–150.

557